Applied Catalysis B: Environmental 189 (2016) 233–241

Contents lists available at ScienceDirect

Applied Catalysis B: Environmental

journal homepage: www.elsevier.com/locate/apcatb

Ni/CeO_2 catalysts for methane partial oxidation: Synthesis driven structural and catalytic effects

G. Pantaleo[a], V. La Parola[a], F. Deganello[a], R.K. Singha[b], R. Bal[b], A.M. Venezia[a,*]

[a] Institute of Nanostructured Materials (ISM N-CNR), Via Ugo La Malfa 153, 90146 Palermo, Italy, Italy
[b] Indian Institute of Petroleum, Dehradun, Uttaranchal, India

ARTICLE INFO

Article history:
Received 18 December 2015
Received in revised form 23 February 2016
Accepted 27 February 2016
Available online 3 March 2016

Keywords:
Methane catalytic partial oxidation (CPO)
CH_4 TPSR
Ni catalysts
CeO_2,

ABSTRACT

Catalytic partial oxidation of methane (CPO) to synthesis gas was performed over differently prepared CeO_2 supported nickel catalysts with 6 wt% Ni content. The samples were synthesized by microwave assisted procedures and by hydrothermal deposition procedure. Differences in the catalyst structural properties of the prepared catalysts were detected by XRD, TPR and XPS measurement. When tested at atmospheric pressure with feed gas mixture containing methane and oxygen in molecular ratio $CH_4/O_2 = 2$, all the samples reached 98% conversion with CO selectivity values >95% in the 700–800 °C temperature range. The samples exhibited different behavior towards carbon formation during the tests. Moreover, according to XRD, XPS and TGA results, when the carbon was formed it did not cause catalyst deactivation. TPR profiles confirmed different degree of chemical interaction between NiO and CeO_2 support, depending on the preparation method. The building up or the easy removal of carbon during the CH_4 temperature programmed surface reaction (TPSR), substantiate the role of the CeO_2 lattice oxygen mobility, enhanced by metal-support interaction, in the removal of the deposited carbon through CO evolution. Structure-activity relationship established a close dependence of the CPO performance on the combination of NiO and CeO_2 crystallite sizes and the interaction between the two.

1. Introduction

Direct transformation of methane into valuable chemicals, such as the oxidative coupling of methane into ethane or direct oxidation of methane to methanol or formaldehydes are not very efficient processes with yield of 30%, 8% and 4% respectively. The most practical way to use methane involves indirect processes through its initial conversion to syngas. Syngas, a mixture of CO and H_2 with different CO/H_2 molar ratio is industrially produced by reforming processes such as steam reforming (SR), dry reforming (DR) and autothermal reforming (ATR), a combination of the endothermic reforming and the exothermic oxidation reactions [1–3]. Catalytic partial oxidation of methane (CPO) would be a better cost and energy efficient way to produce syn gas. It allows 10–15% reduction in the energy requirement and 25–30% lower capital investment as compared to the typical steam reforming processes. Moreover the produced synthesis gas with $H_2/CO = 2$ is suitable for methanol and Fisher Tropsch syntheses [4]. In order to make the process appealing to the industry it is mandatory to develop suitable nickel based catalysts as alternative to the more expensive noble metal ones. Currently the main drawbacks of the nickel catalysts are their tendency to metal sintering and the easy formation of carbon which poisons the catalysts and clogs the reactor. As recently reported, the use of rare earth oxides, such as La_2O_3, CeO_2 and mixture of the two oxides as supports, produced very active nickel catalysts with rather limited carbon formation [5]. As indicated in the literature, CeO_2 is the most suitable material component among the rare earth oxides for several application such as in environmental pollution control, when oxidation reactions are involved, and also in energy related application [6,7]. This versatile use of ceria is attributed to its unique redox features which enables the oxide to act as an excellent oxygen storage material [8]. In particular it was observed that, although nickel did not enter the CeO_2 lattice, a reciprocal influence between NiO and CeO_2, enhanced by a specific preparation procedure would yield smaller NiO and CeO_2 crystallites. Nevertheless if the smaller sizes were beneficial for an increase of the CPO activity at a lower temperature, in a long run the samples with the lowest initial NiO particle sizes exhibited a stronger deactivation which was related to the lower reducibility and to the sintering of nickel [5]. The study also confirmed that the structural properties of the precursor oxide catalysts were crucial for the formation of the carbon and the sintering of the active nickel. Moreover, CeO_2

* Corresponding author.
E-mail address: venezia@pa.ismn.cnr.it (A.M. Venezia).

http://dx.doi.org/10.1016/j.apcatb.2016.02.064
0926-3373/

supported nickel and also unsupported $Ce_{1-x}Ni_xO_y$ for partial oxidation of methane were reported to show the positive effect of the support oxygen mobility particularly in removing the formed carbon [9,10]. According to literature the oxygen storage capacity (OSC) of ceria is strictly related to the crystallite size strongly dependent on the preparation route [11–14]. As documented in literature, the redox process can be triggered by direct electron transfer from a metal or molecule adsorbed over the ceria surface, which would lead to partially positively charged adsorbates and to the reduction of Ce^{4+} to Ce^{3+} [14,15]. It is also reported that the CeO_2 redox property tends to deteriorate at high temperature, due to the sintering of the crystallites inhibiting the rapid exchange between Ce^{3+} and Ce^{4+} and the propagation of the oxygen vacancies to interfacial areas [16].

As a continuation of a previous study [5], the objective of the present work is to understand the effect of the nickel introduction procedure on the CPO activity of CeO_2 supported Ni catalysts in terms of microstructural, structural and redox properties modification. The adopted preparation procedures were chosen to achieve small support crystallite size and small NiO particles with different degree of metal support interaction. The physical chemical properties of the catalysts and their changes during the catalytic reaction were investigated by XRD, XPS, TPR and TGA analyses.

2. Experimental

2.1. Sample preparation

All the reagents were from Aldrich and used without further purification. The nickel loading in all the catalyst was 6 wt% as confirmed by atomic emission spectroscopy.

2.1.1. Support preparation

CeO_2 oxide was prepared following two methods. One consisted in the homogeneous precipitation of the CeO_2 oxide from the nitrate precursor $Ce(NO_3)_3{\cdot}6H_2O$ using dilute (25%) aqueous ammonia according to a published procedure [17,18]. The resulting mixture was stirred for 3 h at 80 °C. Finally, the entire mixture was evaporated to dryness at 100 °C for 12 h. The obtained solid was calcined at 550 °C for 4 h in air, yielding the support labeled as $CeO_2(HP)_{NH4}{}^+$. In the second method, the CeO_2 was obtained by precipitation assisted by microwave irradiation. Typically the procedure consisted in dissolving 5 g of cerium nitrate hexahydrate in 30 ml of ethanol and then adding dropwise NaOH 10 M until pH = 9. Thereafter the obtained slurry was placed inside a conventional household microwave with the power set at 180 W, operated in 30 s cycles (on for 10 s and off for 20 s) for a total irradiation time of 10 min. The collected precipitate was washed with distilled water to remove nitrates and sodium ions, then washed with ethanol, dried at 100 °C for 1 h and then calcined at 800 °C for 2 h yielding $CeO_2(MW)$.

2.1.2. Catalyst preparation

In the different catalyst syntheses the required amount of nickel and ceria precursors were used to yield a final nickel loading of 6 wt%. The nickel catalysts labeled as *Ni/CeO_2(mw-WI)* and *Ni/CeO_2(mw-CP)* were prepared by microwave assisted wet impregnation and co-precipitation. The first sample was prepared by adding 10 ml of aqueous solution of $Ni(NO_3)_2{\cdot}6H_2O$ to a suspension of 2 g of the microwave prepared CeO_2 in 20 ml of ethanol. Then nickel hydroxide was precipitated adding dropwise 10 M NaOH solution until pH = 9. Thereafter the obtained slurry was placed inside a conventional household microwave with settings and microwave exposure time as above. The collected precipitate, washed with distilled water and ethanol, was dried at 100 °C for 1 h and then calcined at 800 °C for 2 h. The co-precipitated sample

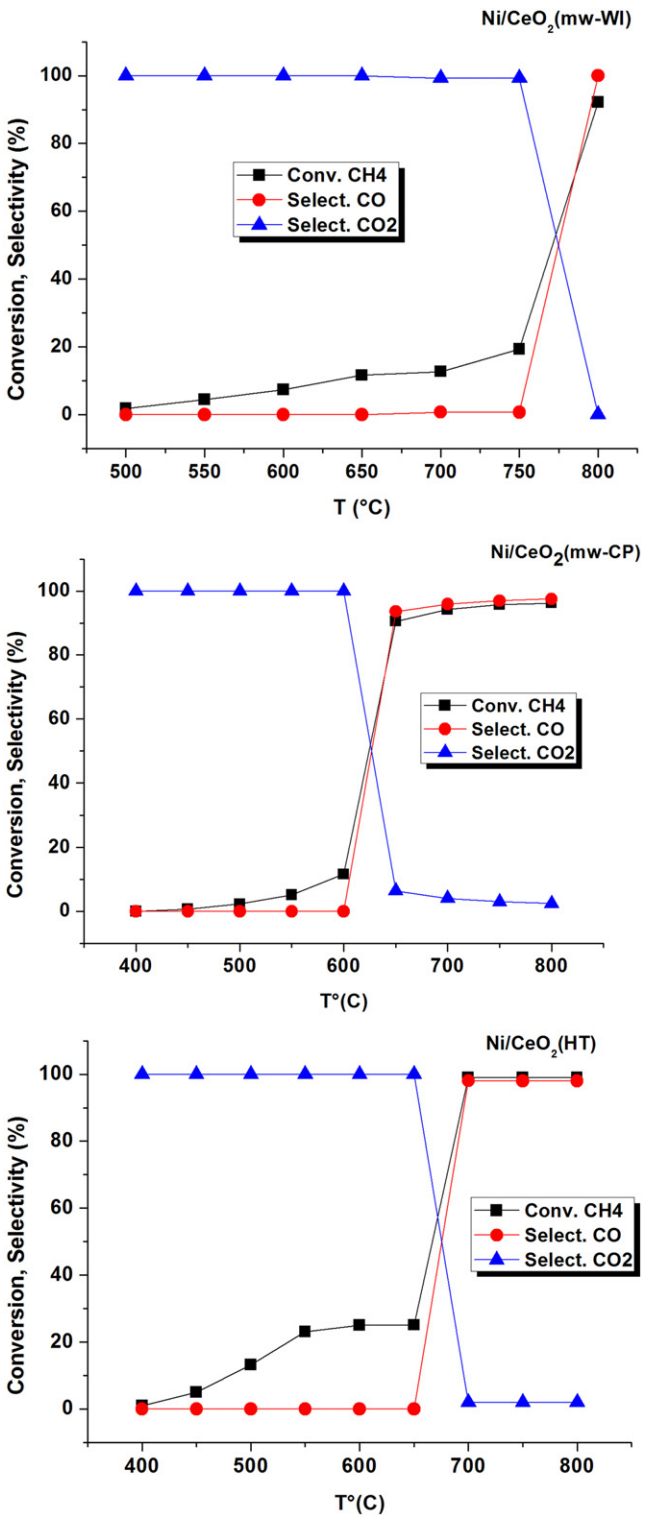

Fig. 1. CH_4 conversion and selectivity to CO and CO_2 as a function of temperature.

Ni/CeO_2(mw-CP) was prepared as the microwave prepared CeO_2 except for adding together the nickel nitrate and the cerium nitrate precursors. The third catalyst, labeled as *Ni/CeO_2(HT)*, was prepared by hydrothermal synthesis previously described [18]. The synthesis consisted in adding together an ethanol solution of cetyltrimethylammonium bromide (CTAB, 1.2 g in 5 ml ethanol) and an aqueous solution of nickel nitrate hexahydrate ($Ni(NO_3)_2{\cdot}6H_2O$, 0.8 g in 5 ml distilled water) and treating it at 100 °C in a Teflon lined stain-

less steel autoclave for 2 h. After cooling to room temperature, the nickel containing solution was added to the previously prepared ceria, $CeO_2(HP)_{NH4}^+$, dispersed in ethanol. The resulting mixture was stirred for 30 min. Hydrazine was added as a chelating agent in order to limit the agglomeration of Ni species. The mixture was then evaporated to dryness at 80 °C overnight. Finally the obtained solid was dried at 100 °C for 3 h followed by calcination at 550 °C for 6 h.

2.2. Sample characterization

The specific surface area of the supports were determined from N_2 adsorption–desorption isotherms at −196 °C using a Sorptomatic 1900 (Carlo Erba) instrument through the Brunauer–Emmett–Teller (BET) calculation methods [19]. Before the measurements, samples were heated in vacuum at 250 °C for 2 h.

The phase composition of crystalline components of fresh and aged samples was investigated by X-ray diffraction (XRD) analyses. The XRD patterns were recorded in Bragg-Brentano para-focusing geometry using a Bruker D5000 diffractometer, equipped with Cu Kα anode and graphite monochromator. The XRD data were collected in the angular range 10°–80° 2θ with 0.05° step size and counting time of 5 s per step. The assignment of the various crystalline phases was based on the JPDS powder diffraction file cards [20]. The diffraction patterns were analysed by Rietveld refinement using the GSAS package [21]. Chebyschev polynomials and Pearson VII functions were chosen for the background and for the peak profile fitting, respectively. In the structure refinement, lattice constants, zero offset, scale factors and full width half maximum (FWHM) were considered as variable parameters. From fitting results, the structural parameters of the investigated compounds and, in particular, the cell edge lengths and the relative phase composition were obtained. An estimation of the mean crystal size values was obtained from the line broadening calculated by Rietveld analysis in agreement with the GSAS package procedure [21] and with the Scherrer equation [22].

Temperature programmed reduction (TPR) experiments were carried out with a Micromeritics Autochem 2950HP apparatus equipped with thermal conductivity detector (TCD). The gas mixture with composition 5% H_2 in Ar (30 ml/min) was used to reduce the samples (50 mg) heating from room temperature to 1050 °C at the rate of 10 °C/min. Before starting the TPR analyses, the catalysts were pretreated with a flowing gas mixture of 5% O_2 in He (50 ml/min) at 350 °C for 30 min, then cooling down under He.

The thermogravimetric analyses (TGA) of the samples after the catalytic reactions were performed in air using the TGA 1 Star System of Mettler Toledo. About 10 mg of sample was heated from room temperature to 1100 °C at the rate of 10 °C/min. The evolution of the CO_2 was monitored by mass quadrupole.

The X-ray photoelectron spectroscopy (XPS) analyses of the calcined and spent catalysts were performed with a VG Microtech ESCA 3000 Multilab, equipped with a dual Mg/Al anode. The spectra were excited by the Mg Kα source (1253.6 eV) run at 14 kV and 15 mA. The analyzer operated in the constant analyser energy (CAE) mode. Survey spectra were measured at 50 eV pass energy. For the individual peak energy regions, a pass energy of 20 eV set across the hemispheres was used. The sample powders were mounted on a double-sided adhesive tape. The pressure in the analysis chamber was in the range of 10^{-8} Torr during data collection. The constant charging of the samples was corrected by referencing all the energies to the C 1s peak energy set at 285.1 eV, arising from adventitious carbon. Contact of the spent catalysts with air was minimized by keeping them under inert gas until being transferred through a glove box into the XPS instrument. Analyses of the peaks were performed with the software provided by VG, based on non-linear least squares fitting program using a weighted sum of Lorentzian and Gaussian component curves after background subtraction according to Shirley and Sherwood [23]. Atomic concentrations were calculated from peak intensity using the sensitivity factors provided with the software. The binding energy values are quoted with a precision of ±0.15 eV and the atomic percentage with a precision of ±10%.

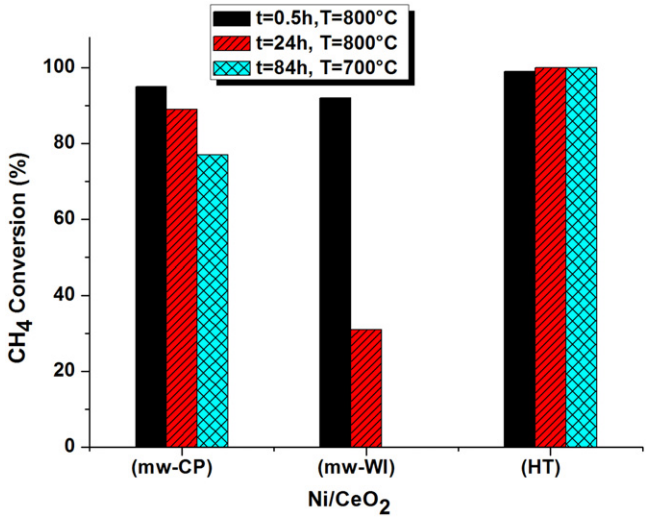

Fig. 2. CH_4 conversion after different time on stream for the differently prepared nickel catalysts.

2.3. Catalytic measurements

Methane oxidation catalytic tests were performed in a U shaped quartz reactor with an inner diameter of 12 mm, using the apparatus already described [5]. The catalyst powder (sieved fraction between 180 and 250 mm) was diluted 1:2 with inert SiC, in order to avoid thermal gradients. Prior to the catalytic testing, the samples were treated "in situ" under flowing O_2 (5 vol.% in He, 50 ml/min) at 350 °C for 1/2 h. After cooling down to room temperature, the samples were reduced under flowing H_2 (5 vol.% in Ar, 30 ml/min) increasing the temperature to 750 °C with a 10 °C/min ramp and a holding time of 1 h. The feed gas consisting of 2 vol.% of CH_4 + 1 vol.% O_2 in He, was led over the catalyst (50 mg) at a flow rate of 50 ml/min (STP), equivalent to a weight hourly space velocity (WHSV) of 60,000 ml g^{-1} h^{-1}. The activities were measured as a function of temperature from 400 °C to 800 °C with a heating rate of 10 °C/min and waiting 30 min for each 50 °C step.

For the long run stability tests the catalytic activity of the samples, kept at the temperature of the maximum conversion for a chosen length of time, was measured. The inlet and outlet gas compositions were analysed by on line mass quadrupole (Thermostar™, Balzers), in order to follow the evolution of all the species, CH_4, CO, CO_2, H_2, H_2O, O_2. Moreover, the accurate concentrations of CO, CO_2 and CH_4 species were obtained by IR analysers (ABB Uras 14, Uras 26), calibrated in the range 0–3000 ppm for CO, 0–10000 ppm for CO_2 and 0–30000 ppm for CH_4. The methane conversion X_{CH4} and the CO selectivity S_{CO} were calculated as $X_{CH4} = (CH_4^{in}\text{-}CH_4^{out})/CH_4^{in} \times 100$ and $S_{CO} = CO/(CO + CO_2) \times 100$. Carbon balance was close to ±5% in all the catalytic tests.

The activation of methane by the catalysts was investigated by temperature-programmed surface reactions (TPSR) performed using the same sample pretreatment and the same experimental conditions as used for the CPO reaction except for the reactant gas being 2 vol% CH_4 in N_2 without oxygen. The evolution of CH_4, CO, CO_2 and H_2 was recorded as function of temperature.

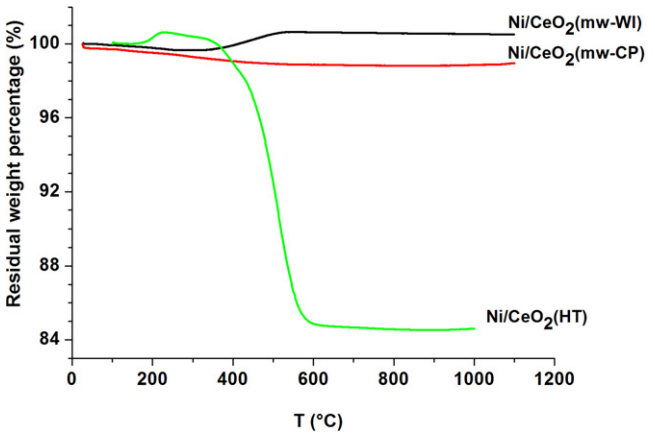

Fig. 3. TGA profiles of differently prepared nickel catalysts after the stability test at 800 °C.

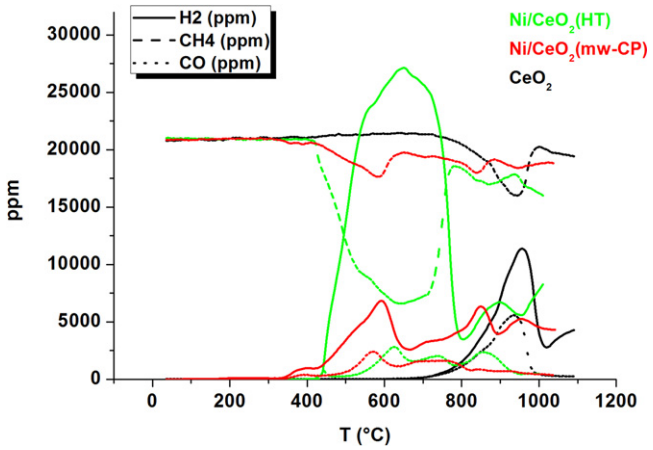

Fig. 4. Methane TPSR over differently prepared nickel catalysts and bare CeO_2 support.

3. Results and discussion

3.1. Catalyst activity and carbon formation

The performance of the three catalysts in terms of methane conversion and product selectivity (CO and CO_2) as function of temperature, is shown in Fig. 1. As already observed before, the low temperature, in the range 450 °C–600 °C, favored the total oxidation of methane which in the case of Ni/CeO_2(HT) sample reached the 25% conversion corresponding to the maximum conversion allowed by the available oxygen [5]. Thereafter an abrupt increase of the CPO activity occurred. In all cases the catalysts achieved high CPO methane conversion and high CO selectivity, close to the thermodynamic equilibrium values [4,5]. In terms of CPO light off temperature, the catalyst prepared by microwave assisted co-precipitation *NiCeO$_2$(mw-CP)* and the catalyst prepared by post hydrothermal synthesis *Ni/CeO$_2$(HT)* are the most active, with the former one exhibiting 90% conversion already at 650 °C. The catalyst stability was checked by monitoring the reaction at the temperature of the maximum CH_4 conversion for selected length of time. The results are summarized in Fig. 2 with a bar diagram of the methane conversion for the different catalysts. The conversions measured after 30 min and after 24 h of reaction at 800 °C are reported for the three catalysts. The activities of *Ni/CeO$_2$(mw-CP)* and *Ni/CeO$_2$(HT)* were also monitored at 700 °C and the corresponding conversion values after 84 h of reaction are also given in Fig. 2. Clearly, the hydrothermal prepared catalyst was the most stable one.

The formation of carbon during the CPO reaction was investigated by thermogravimetry analyses of the aged samples, after the 24 h stability test at 800 °C. The TGA curves are plotted in Fig. 3. The sample weight loss as a function of temperature, coupled with the CO_2 evolution (not shown) detected by the mass quadrupole, reflects the amount of carbon formed during the catalytic test. The small weight gain observed in some cases is likely due to the oxidation of the Ce^{3+} or Ni^{2+} formed in the reducing atmosphere of the CPO reaction [5]. By comparing the TGA curves with the data in Table 1, it is worth to notice that the sample prepared by hydrothermal synthesis, with about 15 wt% weight loss corresponding to the deposited carbon, contains the smallest nickel particles after the reaction. Moreover, in spite of the carbon deposition, the *Ni/CeO$_2$(HT)* was the most stable catalyst. On the contrary, *Ni/CeO$_2$(mw-CP)* and *Ni/CeO$_2$(mw-WI)*, with rather flat TGA curves, underwent metal sintering, especially the *Ni/CeO$_2$(mw-WI)* which drastically deactivated during reaction.

For the two better performing catalysts, the *Ni/CeO$_2$(HT)* and *Ni/CeO$_2$(mw-CP),* their reactivity towards the dissociation of methane with formation of hydrogen and carbon, in the absence of oxygen, was investigated by performing CH_4 temperature programmed surface reaction (TPSR). The desorption profiles in terms of CH_4, H_2 and CO, for the selected catalysts and the bare CeO_2 support, are given in Fig. 4. In all cases the amount of evolved CO_2 was negligible. The curves shown in the figure as related to CeO_2 are characteristic of the two cerium oxides prepared for this study. Comparison of the catalysts and support curves indicates that CeO_2 alone is not able to activate CH_4 at temperature below 730 °C, contrary to the Ni/CeO_2 samples in which the presence of nickel induces methane decomposition at much lower temperature. Moreover, over CeO_2 the methane conversion occurs in a relatively narrow temperature range (730–1000 °C) with stoichiometric formation of H_2 and evolution of CO due to the interaction with the lattice oxygen of ceria [24]. Over the nickel catalysts, the onset for the hydrogen evolution is 410 °C, about 150 °C lower than what reported for similar type of samples but with superior nickel loading [24]. As shown in Fig. 4, quite significant differences in the converted methane and produced H_2 and CO exist between the two differently prepared catalysts. In the case of *Ni/CeO$_2$(HT)* the decomposition reaction takes place in a range of temperature between 418 °C–780 °C. As shown in the figure, the maximum of the methane conversion occurs at 644 °C with about 14,000 ppm of methane being converted, corresponding to 73% of the methane concentration in the flowing gas mixture. The amount of evolved CO is much less than what would be expected from the carbon derived from the dissociated methane. The increasing conversion of methane with formation of H_2 and CO observed above 800 °C is likely due the activation from the bulk ceria and also to the homogeneous thermal decomposition reaction [25]. The curves for the *Ni/CeO$_2$(mw-CP)* sample are quite different, exhibiting a wider temperature range for the methane decomposition, extending between 418 °C–950 °C, with two peaks centred at 580 °C and at 840 °C corresponding to methane conversion of 14% and 10% respectively. Such peaks reflect different active sites, which may be related to nickel particles of dissimilar sizes or interacting in a different way with the support. Moreover, as observed for the bare CeO_2 but at variance with the *Ni/CeO$_2$(HT)* catalyst, approximately stoichiometric amount of H_2 and CO are produced. The different CO evolution detected for the two catalysts is a clear evidence of a much lower oxygen mobility in *Ni/CeO$_2$(HT)* as compared to the *Ni/CeO$_2$(mw-CP)* [24]. It is worth to notice the capability of methane to extract oxygen from the catalysts with consequent CO formation, below the temperature of the previous reduction treatment at 750 °C. Excluding any kind of gas contamination (indeed no CO was detected during the TPSR with bare CeO_2) the superior reduction capability

Table 1
Specific surface area (BET), nickel phases and ceria crystallite sizes (d) with phase percentages (wt%) in parentheses and CeO_2 lattice parameter (a).

Samples	BET (m^2/g)	Ni phases crystallite size d(nm)[a]		Support crystallite size d(nm)[a]		Lattice parameter a(Å) [a]
		Fresh NiO	Aged Ni	Fresh CeO_2	Aged CeO_2	Fresh CeO_2
Support						
CeO_2(mw)	30			30		5.411
$CeO_2(HP)_{NH4}^+$	38			17		5.410
Catalyst						
Ni/CeO_2(mw-CP)	26	18 < *d* < 40(3)	20 < *d* < 70(3)	13(97)	13(97)	5.412
Ni/CeO_2(mw-WI)	26	28(9)	105(10)	30(91)	32(90)	5.411
Ni/CeO_2(HT)	28	28(6)	25 (6)	14(94)	33(94)	5.409

[a] Calculated by the Rietveld refinement analysis.

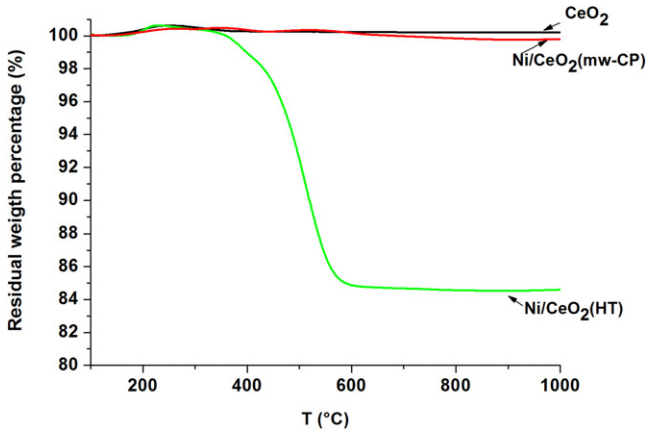

Fig. 5. TGA profiles of nickel catalysts after CH_4 decomposition test.

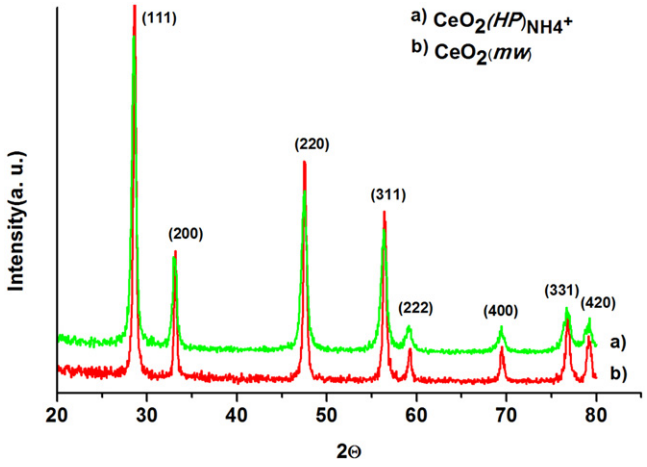

Fig. 6. XRD patterns of the two differently prepared CeO_2 supports.

of methane with respect to hydrogen is explained by the different type of reduction processes occurring with H_2 and CH_4. In the first case, H_2 acts over the oxidized catalysts as a direct reducing agent. In the second case, methane, activated by metallic nickel, is first decomposed to carbon and hydrogen. Then the deposited carbon reacts with the ceria lattice oxygen which, according to the TPR at the 750 °C, has still plenty of reducible Ce^{+4} with oxygen vacancy creation.

The carbon build-up over the samples after the methane decomposition was checked by TGA analyses. The obtained profiles shown in Fig. 5 are in perfect agreement with the TPSR results of Fig. 4 discussed above. Indeed, opposite to the TGA flat curves of *CeO_2* and *Ni/CeO_2(mw-CP)* samples, evolving CO during TPSR, a weight loss corresponding to deposited carbon is observed only with *Ni/CeO_2(HT)* catalyst.

3.2. Characterization

3.2.1. XRD analyses

The structural parameters of the supports and catalysts obtained from the Rietveld analyses of the XRD patterns are listed in Table 1, along with the specific surface area determined by the BET method. The two samples of cerium oxide are characterized by slightly different surface areas, although larger differences would have been expected in consideration of the different calcination temperatures, 800 °C for the *CeO_2(mw)* and 550 °C for the *$CeO_2(HP)_{NH4+}$*. Consistent surface area values are found for the corresponding nickel catalysts. The XRD patterns of the two CeO_2 samples are shown in Fig. 6. As given in Table 1, the XRD derived CeO_2 crystallite size in *$CeO_2(HP)_{NH4+}$* is quite smaller as compared to the *CeO_2 (mw)*, as expected from the different calcination temperatures.

In order to correlate the activity with the structural properties, X-ray diffraction analyses of the differently prepared nickel catalysts were performed on fresh (calcined) and on aged (after the stability test of CPO at 800 °C) samples. In the XRD patterns, given in Fig. 7, weak reflections attributed to NiO in the calcined samples and to Ni in the aged samples together with the main reflections of the cubic CeO_2 are generally present. In some cases such as in patterns (e) and (f) referring to *Ni/CeO_2(mw-CP)* the nickel phase peaks were not discernable. Generally Rietveld refinement allowed to obtain crystal sizes with a certain degree of confidence, except for the data of the two cited patterns for which the Rietveld refinement, due to the low amount of crystalline nickel phase, did not allow to obtain reliable values and only a rough estimate for the nickel crystallite sizes is given in Table 1. The small feature in pattern (d) located at $2\theta \sim 32°$ arises from unidentified impurity. As reported in Table 1, the NiO and CeO_2 crystallite sizes of the fresh samples are all reasonably small, however, after the catalytic test, the size of the NiO crystallites ends up in different metallic nickel crystallite sizes. A significant crystallite size growth occurs in *Ni/CeO_2(mw-WI)* sample, whereas just a limited size enlargement is observed in *Ni/CeO_2(mw-CP)* likely due to the more intimate contact between nickel and CeO_2 achieved during the co-precipitation synthesis [5]. On the contrary stable crystallites are detected in *Ni/CeO_2(HT)*. For this latter sample, where, according to TPR, NiO is not interacting with the support, it is not excluded that the use of a templating agent during the impregnation of the ceria with the nickel precursor may have contributed to maintain the nickel crystallites quite small during the CPO reaction. However, as previously reported for similar type of catalysts, the carbon, deposited during the catalytic test, as confirmed by the TGA analysis, might inhibit crystal growth [5].

The sizes of the CeO_2 crystallites in the different catalysts do not change significantly after the reaction, except in the *Ni/CeO_2(HT)* exhibiting a certain increase, indicative of a weaker nickel-support interaction [5]. According to Table 1, the value of the CeO_2 lattice parameter is not appreciably influenced by the presence of nickel.

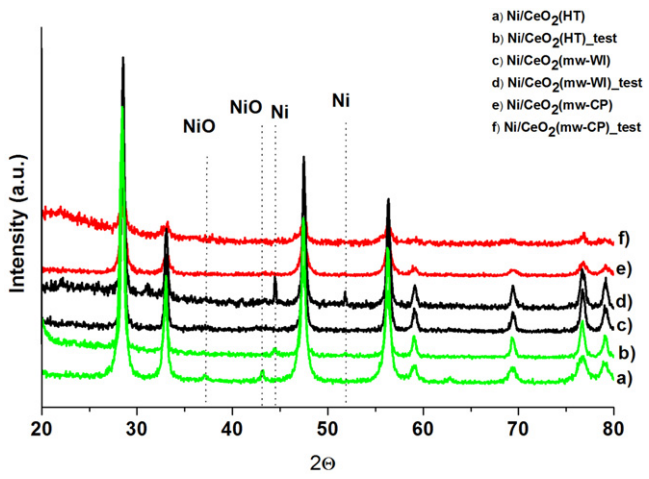

Fig. 7. XRD patterns of the differently prepared nickel catalysts.

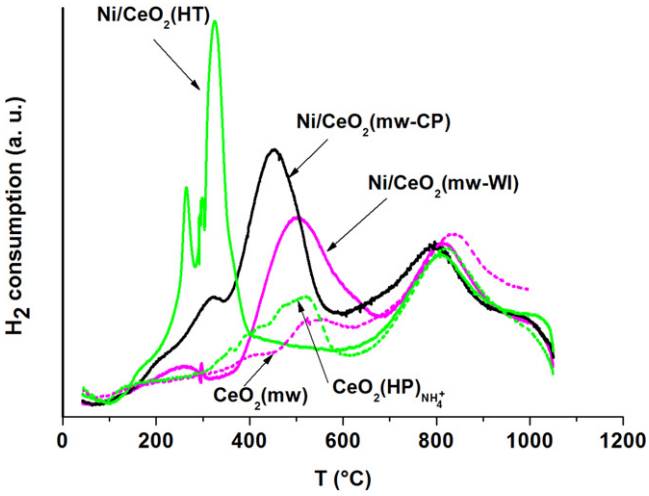

Fig. 8. TPR profiles of the differently prepared nickel catalysts and corresponding supports.

However, if the introduction of Ni into the CeO_2 lattice should cause a decrease of the lattice parameter due to the smaller radius of Ni^{2+} (0.69 Å) as compared to the Ce^{4+} (0.97 Å), at the same time it would generate new oxygen vacancies inducing a small expansion of the cell. As a consequence, the two effects would cancel out and therefore no indication of a real insertion of nickel ions into the ceria lattice can be ascertained [26].

3.2.2. TPR analyses

The temperature programmed reduction profiles shown in Fig. 8 give information on the relative oxygen storage capacity (OSC) of the different nickel catalysts and corresponding ceria supports. As known from literature the TPR of CeO_2 is generally characterized by a reduction peak centred at about 800 °C attributed to the reduction of bulk ceria and by a low temperature peak, attributed to the release of oxygen from the surface of ceria. In the present study the high temperature peak is found at ~830 °C. Moreover, both CeO_2 profiles present a broad feature peaked at ~530 °C corresponding to the reduction of the surface ceria [7,27]. The small differences observed between the TPR profiles of the two cerium oxides in terms of peak temperature and hydrogen consumption are expected. Indeed, in the absence of supported metal, the H_2 activation on the surface is the rate-limiting step for the reduction process and therefore any small variations in the support surface area and crystallite sizes can affect the redox behavior [11,12]. As shown in Fig. 8 the addition of nickel modifies the TPR profiles to different extent depending on the preparation method. The profiles are quite dissimilar from those obtained previously for two classically prepared Ni/CeO_2 exhibiting peaks clearly attributable to the reduction of NiO [5]. As expected all the samples give rise to the high temperature peak due to the bulk CeO_2 reduction. With respect to *Ni/CeO$_2$(mw-CP)* and *Ni/CeO$_2$(mw-WI)* their TPR profiles are characterized by a quite broad peak with a maximum at 450 °C and 506 °C respectively, overlapping with the temperature region of the surface ceria reduction. The TPR profile of the sample *Ni/CeO$_2$(HT)*, contains two peaks, one at 262 °C and the other at 327 °C. The position of these peaks is more typical of NiO reduction peaks [5,27]. The results from the TPR analyses in terms of reduction peak temperatures and hydrogen consumption volumes are listed in Table 2. During TPR, the bare CeO_2 is reduced according to the following equation:

$$2CeO_2 + H_2 = Ce_2O_3 + H_2O \quad (1)$$

From the hydrogen consumption listed in Table 2, obtained by the integration of the peak areas, it is possible to evaluate the percentage of reduction and to roughly estimate the average "*x*" value in CeO_{2-x}. It is indeed known that there are different kinds of nonstoichiometric cerium oxide between CeO_2 and Ce_2O_3 [28]. It follows that the *CeO$_2$(HP)$_{NH4}^+$* and the *CeO$_2$(MW)* consuming a total of 38 ml/g and 33 ml/g of H_2 individually, are reduced by 54% and 47%, consistent with nonstoichiometric oxides $CeO_{1.77}$ and $CeO_{1.73}$ respectively. On the bases of the two cerium species concentration $[Ce^{3+}]$ and $[Ce^{4+}]$ as estimated from the TPR, the corresponding oxygen vacancy is calculated according to the formula

$$[V_O] = 1 - (3[Ce^{3+}] + 4[Ce^{4+}])/4 \quad (2)$$

The obtained values of V_O are 11% for *CeO$_2$(HP)$_{NH4}^+$* and 13% for *CeO$_2$(MW)* [29]. The 6 wt% analytical loading of nickel corresponds to 0.00103 mol per grams. According to the 1:1 stoichiometry, the complete reduction of Ni^{2+} should require 23 ml/g of H_2. As shown in Fig. 8 and Table 2, the temperature programmed reduction of the microwave assisted catalysts gives rise to rather modest hydrogen consumption at low temperature (260–320 °C). The corresponding H_2 volumes are in fact less than what the total nickel reduction would require. It is therefore plausible that the large and broad hydrogen consumption peaks, closer in temperature to the surface ceria peak of the bare support, contain the contribution from NiO and surface ceria reduction. Moreover, their shift to a lower temperature with respect to the CeO_2 surface peak (at 538 °C for *CeO$_2$(MW)* and 517 °C for the *CeO$_2$(HP)$_{NH4}^+$*) is indicative of an intimate contact between nickel and ceria enhancing the oxygen mobility [15]. The broadness of the feature is in accord with the presence of a distribution of species reducing in a wide range of temperature without a definite interface between supported metal and ceria surface. The TPR pattern of the *Ni/CeO$_2$(HT)* sample presents two low temperature peaks, one at 262 °C and the other at 327 °C both quite narrow, attributable to the reduction of NiO particles of slightly different size [5]. According to the H_2 volume consumption, the all feature may include also some small contribution from the surface ceria reduction. On the bases of the hydrogen consumption, using the same calculation as for the pure supports, the ceria oxygen vacancy concentration was also estimated for the catalysts. The obtained values are listed in Table 2. Within the error of the H_2 volume ascription to each TPR peaks, overall, the addition of nickel increases slightly the oxygen vacancy concentration in accord with charge compensation effect [15].

3.2.3. XPS analyses

The surfaces of the samples were investigated by X-ray photoelectron spectroscopy. The results are summarized in Table 3 in

Table 2
T_{max} and H_2 consumption volumes (V) of the TPR peaks obtained for the CeO_2 supports and Ni catalysts. The concentration (%) of the oxygen vacancy (Vo) estimated by eq. (2) for each sample is listed.

Sample	T_{max}(°C)			V (ml/g_{catal})			V_O (%)[a]
	1st peak	2nd peak	3rd peak	1st peak	2nd peak	3rd peak	
Support							
CeO_2 (mw)		538	840		6	27	13
CeO_2 (HP)$_{NH4+}$		517	823		14	24	11
Catalyst							
Ni/CeO_2(mw-CP)	320	450	796	4	26	22	15
Ni/CeO_2(mw-WI)	265	505	811	3	26	24	14
Ni/CeO_2(HT)	262	327	807	7	20	23	13

[a] The values for the catalysts have been obtained assuming that the NiO reduction required the H_2 volume of 23 ml/g for each sample.

Table 3
Main XP binding energies and XPS derived atomic ratio of the various Ni catalysts in the calcined state.

Samples	Ni $2p_{3/2}$	Ce $3d_{5/2}$ (V)	O1s (at%)[a]	Ni/Ce[b]	Ce^{3+}/Ce_{tot}[b]	C/Ni[b]
Ni/CeO_2(mw-CP)	855.2	882.4	529.7(74%) 532.0(26%)	0.16 (0.12)	0.10 (0.28)	28 (70)
Ni/CeO_2(mw-WI)	855.1	882.1	529.5(58%) 531.8(42%)	0.43 (0.10)	0.06 (0.21)	29 (120)
Ni/CeO_2(HT)	855.1, 853.2	881.9	529.4(84%) 531.7(16%)	0.31(0.08)	0.11 (0.17)	23 (520)

[a] Relative atomic concentration.
[b] The values in parentheses refer to the samples after the stability test at 800 °C of the CPO reaction.

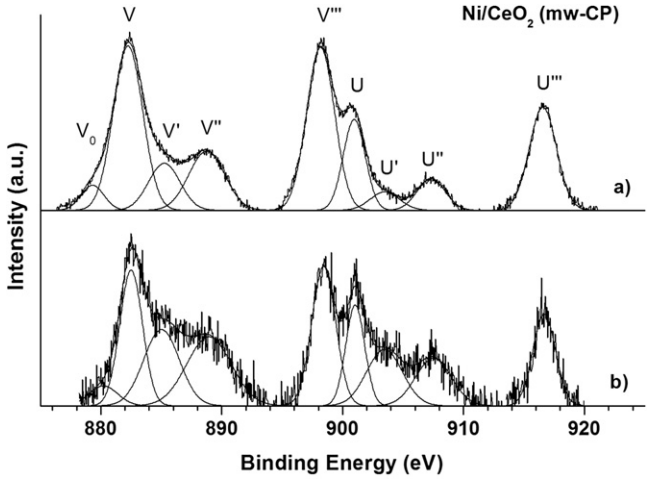

Fig. 9. Experimental and fitted Ce 3d XP spectra of: (a) before; (b) after catalytic test.

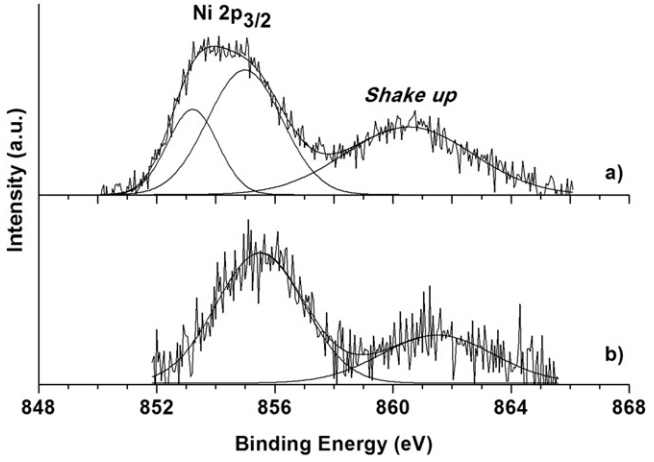

Fig. 10. Experimental and fitted Ni $2p_{3/2}$ XP spectra of calcined catalysts: (a) Ni/CeO_2(HT); (b) Ni/CeO_2(mw-CP).

terms of the main photoelectron lines, Ni $2p_{3/2}$, Ce $3d_{5/2}$ (V component), O 1s, and atomic ratios. Typical Ce 3d core level spectra of a selected sample, *Ni/CeO_2(mw-CP)*, before and after the stability test of the CPO reaction are shown in Fig. 9. The spectra from the Ce^{4+} chemical state are characterized by the spin orbit photoelectron peaks Ce $3d_{5/2}$ and Ce $3d_{3/2}$ with multiple components, labeled as V, V", V"' and U, U", U"' respectively, arising from the transition to different final states. Moreover, beside the peaks due to the Ce^{4+} species, the components V_0, V' and U' referring to Ce^{3+} chemical state are also present [30]. The percentages of Ce^{3+} with respect to the total Ce concentration are given for the catalysts before and after the reaction in Table 3. The Ce^{3+} ions, detected also in the calcined samples, are in part due to the defective structure of the CeO_2, enhanced by the interaction between the Ni cation and the CeO_2 surface and in part due to the high vacuum and X-ray induced reduction inside the XPS apparatus [15,31]. In the samples analysed after the partial oxidation of methane, a significant increase of the atomic ratio Ce^{3+}/Ce_{tot} is obtained for the two microwave prepared catalysts. The limited increase of this ratio in the case of the *Ni/CeO_2 (HT)* sample is once more suggestive of a lower oxygen mobility, as discussed above [24]. The Ni $2p_{3/2}$ photoelectron spectrum is shown in Fig. 10 for the fresh samples, *Ni/CeO_2(HT)* and *Ni/CeO_2(mw-CP)*. The spectra are typical of NiO with the main Ni $2p_{3/2}$ at 855.1 eV (±0.1) and the shake up satellite at about 861 eV [32]. Given the broadness of the peak some contribution from $Ni(OH)_2$ is also expected. In the case of the *Ni/CeO_2(HT,* the experimental curve clearly contained two components, one typical of NiO oxide, and the other down energy shifted at 853.6 eV indicative of a reduced nickel. As reported in Table 3, the atomic ratio Ni/Ce obtained for the *Ni/CeO_2(mw-CP)* sample is close to the analytical ratio of 0.2. As expected, the ratio is larger for the other two catalysts prepared both by two kinds of metal impregnation. After the catalytic test the Ni/Ce ratio diminishes to various extent. Such decrease may originate from sintering of the nickel particle, or from carbon preferentially deposited over the nickel species. In particular the significant ratio variation of the *NiCeO_2(mw-WI)* is largely due to sintering, in accord with the XRD data in Table 1, whereas the variation in *NiCeO_2(HT)* must be attributed to the

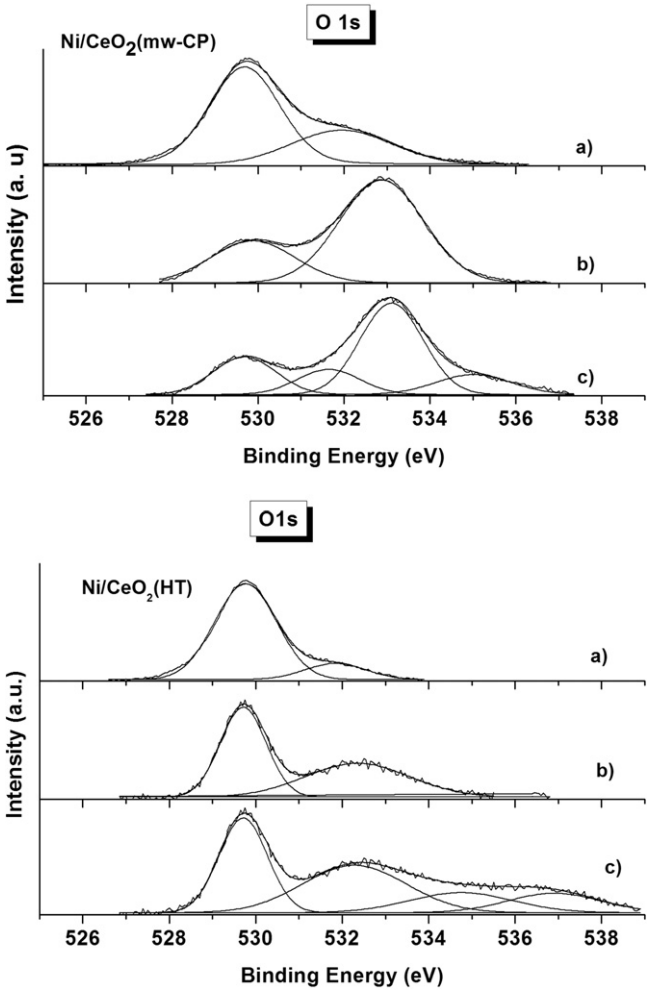

Fig. 11. Experimental and fitted XP O1s spectra of two selected nickel catalysts: (a) before; (b) after CPO test; (c) after methane TPSR.

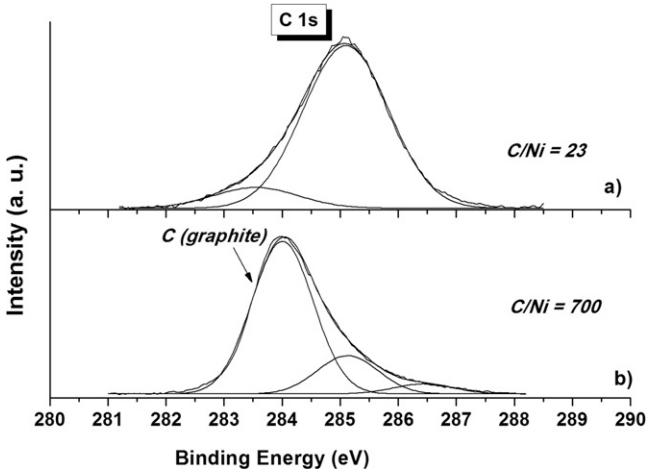

Fig. 12. Experimental and fitted XP spectra of C1s: (a) before; (b) after methane TPSR.

carbon deposition. In fact, even assuming the presence of nickel over the carbon filament tip, the partial covering of nickel by other forms of carbon is generally expected [33]. Concerning the *NiCeO$_2$(mw-CP)* the small atomic ratio variation reflects the slight increase of the nickel crystallite size.

In Fig. 11 the O 1s spectra of the two samples, the Ni/CeO$_2$*(mw-CP)* and the *Ni/CeO$_2$(HT)*, after different stages of the catalyst life are shown. The spectra of the fresh catalysts (Fig. 11a) exhibit two main components one at 529.6 eV (± 0.1) eV attributed to NiO and CeO$_2$ and the other at 531.8 (±0.1) eV related to hydroxyl groups. In the *Ni/CeO$_2$(mw-CP)* sample, according to the spectrum in Fig. 11b, the catalytic reaction induces a relative decrease of the O 1s component attributed to the oxides with respect to the hydroxyl component. Such variation reflects the modification of the surface oxide structure with formation of oxygen vacancy. The binding energy shift of the hydroxyl peak to 532.8 eV is in accord with OH groups strongly interacting with Ce^{3+} surface defects [30]. Moreover the shape of the O 1s spectrum taken after the TPSR (Fig. 11c) is similar to the one after the CPO reaction, except for the presence of weak components at higher binding energy due to Ce^{3+}- related surface defects [24]. Such additional defects are indeed due to the more drastic conditions of the methane dissociation in the absence of oxygen which would further enhance the support oxygen depletion. The O 1s spectrum of the *Ni/CeO$_2$(HT)* sample does not change appreciably upon the CPO and the TPSR reactions, implying a limited participation of the ceria oxygen to the reaction. Following methane decomposition, some additional high temperature peaks related to surface defects are also present.

The C/Ni XPS derived atomic ratios obtained for the fresh and the aged samples after the CPO stability test at 800 °C are listed also in Table 3. In accord with TGA results a substantial increase of the carbon is detected in the aged *Ni/CeO$_2$(HT)* sample. A more drastic change in terms of binding energy and relative intensity was observed for the C 1s spectrum upon the TPSR reaction. Indeed in Fig. 12 the C 1s spectra of the selected sample *Ni/CeO$_2$(HT)* before and after the methane decomposition test, are shown. The corresponding C/Ni atomic ratios are also indicated. Before the test, the typical C 1s peak at 285.1 eV due to the adventitious carbon is obtained. The extra component at the low energy side is attributed to a Ce 4s satellite peak. After the TPSR, the C 1s peak is shifted to ~284 eV, exhibiting an asymmetric tail on the high energy side curve-fitted with the adventitious and some oxidized carbon components. The main peak is typical of graphitic carbon (sp^2) and confirms the deposition of carbon during the decomposition of methane, in accord with the results of Figs. 4 and 5. It is worth noticing the significant increase of the C/Ni atomic ratio upon catalytic methane decomposition.

To summarize, the sample *Ni/CeO$_2$(HT)* prepared by the post synthesis hydrothermal procedure is the most active at 700 °C and also the most stable during long time runs at 700 °C and 800 °C followed by the sample *Ni/CeO$_2$(mw-CP)* active at 650 °C but deactivating during the long time runs. According to the TGA results, graphitic carbon is formed during CPO reaction over *Ni/CeO$_2$(HT)*, without causing catalyst deactivation at least during the monitored reaction period. As derived from the X-ray analyses, this catalyst maintains small nickel particle size, opposite to the other two microwave prepared catalysts, which do not form carbon but have tendency towards nickel sintering. It is worth to notice how the different syntheses lead to structurally different catalysts. Indeed the preparation method of *Ni/CeO$_2$(HT)*, consisting of a sort of impregnation in the presence of an organic polymer and hydrazine, is a soft procedure allowing to obtain small crystallites of NiO and CeO$_2$ not interacting with each other. The two microwave assisted procedures, although quite different, being essentially one impregnation and the other co-precipitation, afford also small crystallites of NiO and CeO$_2$ which, as shown by TPR profiles, are interacting with each other.

Concerning the role of CeO$_2$, as confirmed by TPSR test, it is clear that the support alone activates the methane at quite higher temperature as compared to the supported catalysts, but, depending on the catalyst preparation procedure, it influences differently

the activity of the nickel sites. Indeed, by comparing the two most promising samples, a remarkably high methane decomposition conversion is observed with the *Ni/CeO$_2$(HT)* catalyst, accompanied by some CO evolution and by significant amount of deposited carbon, also observed after the CPO test. The catalytic stability of this catalyst, in spite of the carbon deposition, can be partially explained, based on literature reports, by assuming that among the mechanisms of carbon deposition, the one of carbon filament growth, leaving the nickel on the filament tip and therefore free of any poisoning effects could prevail [33]. On the contrary, the *Ni/CeO$_2$(mw-WI)* and to a lower extent *Ni/CeO$_2$(mw-CP)* deactivate during CPO reaction, in spite of the fact that carbon buildup is not observed. The stoichiometric evolution of CO during the TPSR over the *Ni/CeO$_2$(mw-CP)* is a consequence of the stronger interaction between NiO and CeO_2. Indeed such interaction enhances the ceria oxygen mobility providing the oxygen to remove carbon as CO. As previously reported, the easy removal of carbon during the catalytic test seems to be related to the enhanced sintering of the nickel particles with the consequent long term instability [5].

4. Conclusion

Nickel catalysts supported over ceria are confirmed to be suitable catalysts for the methane CPO reaction. The crystallite sizes and the interaction between NiO and CeO_2 regulated by different catalyst preparation procedures are determinant factors for the activity and for the stability during the reaction. The achievement of small size NiO crystallites, not necessarily interacting with the support, is highly beneficial for the catalytic activity. Moreover, the interaction between NiO and support, by increasing the ceria oxygen mobility, favors the carbon removal. It is worth noticing that although, in the present study, the deposited carbon does not seem to have a direct poisoning effect, its presence is considered highly detrimental for the operation of the actual CPO reactors. In conclusion the design of appropriate catalysts for industrial CPO application where the high activity, high stability with no carbon buildup are needed, should then take into account the right balance between the two different factors.

Acknowledgments

The Bilateral Collaboration Program supported by Italian CNR and Indian CSIR is kindly acknowledged. Dr. Francesco Giordano is kindly acknowledged for performing the XRD analyses.

References

[1] H. Wu, V. La Parola, G. Pantaleo, F. Puleo, A.M. Venezia, L.F. Liotta, Catalysts 3 (2013) 563–583.
[2] M.-S. Fan, A.Z. Abdullah, S. Bhatia, Chem. Sus. Chem. 4 (2011) 1643–1653.
[3] A. Heinzel, B. Vogel, P. Hubner, J. Power Source 105 (2002) 202–207.
[4] S.A. Al-Sayari, Open Catal. J. 6 (2013) 17–28.
[5] G. Pantaleo, V.La Parola, F. Deganello, P. Calatozzo, R. Bal, A.M. Venezia, Appl. Catal. B 164 (2015) 135–143.
[6] D. Valechha, S. Lokhande, M. Klementova, J. Subrt, S. Rayalu, N. Labhsetwar, J. Mater. Chem. 21 (2011) 3718–3725.
[7] N.K. Renuka, N. Harsha, D. Divya, RSC Adv. 5 (2015) 38837–38841.
[8] A.M. Venezia, L.F. Liotta, G. Pantaleo, A. Longo, in: A. Trovarelli, P. Fornasiero (Eds.), Catalysis by Ceria and Related Materials, Ch 12, 2nd ed., Imperial College Press, London, 2013.
[9] W. Shan, M. Fleys, F. Lapicque, D. Swierczynski, A. Kiennemann, Y. Simon, P.-M. Marquaire, Appl. Catal. A 311 (2006) 24–33.
[10] T. Zhu, M. Flytzani-Stephanopoulos, Appl. Catal. A 208 (2001) 402–417.
[11] Y. Namai, K. Fukui, Y. Iwasawa, J. Phys. Chem. B 107 (2003) 11666–11673.
[12] J. Xu, J. Harmer, G. Li, T. Chapman, P. Collier, S. Longworth, S. Chi Tsang, Chem. Commun. 46 (2010) 1887–1889.
[13] J. Kullgren, K. Hermansson, P. Broqvist, J. Phys. Chem. Lett. 4 (2013) 604–608.
[14] B.M. Reddy, T.V. Kumar, N. Durgasri, in: A. Trovarelli, P. Fornasiero (Eds.), Catalysis by Ceria and Related Materials, Ch 8, 2nd ed., Imperial College Press, London, 2013.
[15] M. Nolan, J. Chem. Phys. 136 (2012) 134703–134709.
[16] A. Hornés, A.B. Hungrıa, P. Bera, A. Lopez Camara, M. Fernandez-Garcıa, A. Martınez-Arias, L. Barrio, M. Estrella, G. Zhou, J.J. Fonseca, J.C. Hanson, J.A. Rodriguez, J. Am. Chem. Soc. 132 (2010), 35–35.
[17] N.K. Renuka, J. Alloys Compd. 513 (2012) 230.
[18] R.K. Singha, A. Shukla, S. Adak, C. Pende, S. Saran, R. Bal, Indian J. Chem. 53A (2014) 467–471.
[19] S.J. Gregg, K.S. Sing, Adsorption, Surface Area and Porosity, 2nd ed., Academic Press, San Diego, 1982.
[20] JCPDS Powder Diffraction File Int. Centre for Diffraction Data Swarthmore. 1989.
[21] A.C. Larson, R.B. von Dreele, 'GSAS, the General Structure Analysis System', Los Alamos National Laboratory, 1991, 2016.
[22] H.P. Klug, L.E. Alexander, X-ray Diffraction Procedures for Polycrystalline and Amorphous Materials, Wiley, New York, 1954.
[23] P.M.A. Sherwood, in: D. Briggs, M.P. Seah (Eds.), Practical Surface Analysis, Wiley, New York, 1990, p. 181.
[24] Y. Li, B. Zhang, X. Tang, Y. Xu, W. Shen, Catal. Commun. 7 (2006) 380–386.
[25] M. Younessi-Sinaki, E.A. Matida, F. Hamdullahpur, Intern. J. Hydrogen Energy 34 (2009) 3710–3716.
[26] W. Qi, n K. Xie, M. Liu, G. Wiu, Y. Wang, Y. Zhang, RSC Adv. 4 (2014) 40494–40504.
[27] A.M. Diskin, R.H. Cunningham, R.M. Ormerod, Catal. Today 46 (1998) 147–154.
[28] M. Haneda, T. Mizushima, N. Kakuta, J. Phys. Chem. B 102 (1998) 6579–6587.
[29] S. Chen, L. Li, W. Hu, X. Huang, Q. Li, Y. Xu, Y. Zuo, G. Li, Appl. Mater. Interfaces 7 (2015) 22999–23007.
[30] A. Pfau, K.D. Schierbaum, Surf. Sci. 321 (1994) 71–80.
[31] E. Paparazzo, G.M. Ingo, N. Zacchetti, J. Vac. Sci. Technol. A 9 (1991) 1416.
[32] P. Prieto, V. Nistor, K. Nouneh, M. Oyama, M. Abd-Leftil, R. Diaz, Appl. Surf. Sci. 258 (2012) 8807–8813.
[33] T.V. Reshetenko, L.B. Avdeeva, Z.R. Ismagilov, A.L. Chuvilin, V.A. Ushakov, Appl. Catal. A 247 (2003) 51–63.